AIAA JOURNAL
Vol. 48, No. 1, January 2010

Microramps Upstream of an Oblique-Shock/Boundary-Layer Interaction

S. Lee*
University of Illinois at Urbana–Champaign, Urbana, Illinois 61801
M. K. Goettke†
U.S. Air Force Research Laboratory, Dayton, Ohio 45433
E. Loth‡
University of Illinois at Urbana–Champaign, Urbana, Illinois 61801
and
J. Tinapple§ and John Benek¶
U.S. Air Force Research Laboratory, Dayton, Ohio 45433

DOI: 10.2514/1.41776

To examine the potential of micro vortex generators for shock/boundary-layer interaction control, a detailed experimental and computational study in a supersonic boundary layer at $M = 3.0$ was undertaken. The experiments employed a flat-plate boundary layer with an impinging oblique shock with downstream total-pressure measurements. The moderate Reynolds number of 3800 allowed the computations to use monotone-integrated large eddy simulations. The monotone-integrated large eddy simulations predictions indicated that the shock changes the structure of the turbulent eddies and the primary vortices generated from the microramp. Furthermore, they generally reproduced the experimentally obtained mean velocity profiles, unlike similarly resolved Reynolds-averaged Navier–Stokes computations. The experiments and monotone-integrated large eddy simulations results indicate that the microramps, for which the height is $h \approx 0.5\delta$, can significantly reduce boundary-layer thickness and improve downstream boundary-layer health as measured by the incompressible shape function H. Regions directly behind the ramp centerline tended to have increased boundary-layer thickness, indicating the significant three-dimensionality of the flowfield. Compared with baseline sizes, smaller microramps yielded improved total-pressure recovery. Moving the smaller ramps closer to the shock interaction also reduced the displacement thickness and the separated area. This effect is attributed to decreased wave drag and the closer proximity of the vortex pairs to the wall.

Nomenclature

A_{sep}	=	separation area
a	=	speed of sound
c	=	cord length of the microramp
D	=	width of the computational domain
d	=	width of the microramp
dt	=	differential time
dx	=	differential length in the streamwise direction
dy	=	differential length in the normal direction
dz	=	differential length in the spanwise direction
E	=	height of the computational domain
H	=	incompressible shape factor
h	=	microramp height
L	=	length of the computational domain
M	=	Mach number
P	=	pressure
P_o	=	total pressure
Re_{ref}	=	Reynolds number based on δ^*_{ref}
s	=	spacing between adjacent microramps at the centerline
T	=	temperature
t	=	fluid convection time scale
U	=	average streamwise velocity
U_τ	=	frictional velocity
u	=	instantaneous streamwise velocity
u'	=	streamwise fluctuation the velocity
v	=	normal velocity
w	=	spanwise velocity
W	=	weighting function
x	=	streamwise distance
y	=	normal distance relative to solid wall
z	=	spanwise distance relative to center of domain
α	=	total-pressure recovery factor
β	=	frictional velocity ratio
γ	=	specific heat ratio
Δt	=	time step
Δx	=	streamwise length of the computational cell
δ	=	boundary-layer thickness
δ^*_{ref}	=	displacement thickness at $x = 0$ but with no shock effects
ζ	=	k direction in the computational domain
η	=	wall normal coordinate normalized by boundary-layer thickness
κ	=	von Kármán constant
ξ	=	i direction in the computational domain
τ	=	integration time
τ^*	=	integration time normalized by the freestream flow convection time
υ_ω	=	kinematic viscosity at wall
ψ	=	j direction in the computational domain

Presented as Paper 3916 at the 25th AIAA Applied Aerodynamics Conference, Miami, FL, 25–28 June 2007; received 24 October 2008; revision received 7 July 2009; accepted for publication 10 July 2009.

*Research Assistant, Department of Aerospace Engineering. Member AIAA.
†Aerospace Engineer, Air Vehicles Directorate. Member AIAA.
‡Professor, Department of Aerospace Engineering. Associate Fellow AIAA.
§Mechanical Engineer, Air Vehicles Directorate. Member AIAA.
¶Director, CFD Branch. Fellow AIAA.

Subscripts

dom	=	domain
eddy	=	turbulent eddies
exit	=	domain exit
f	=	total integration time required for final convergence
i	=	initial value
inlet	=	upstream plane used as input for recycling
int	=	total integration time
MP	=	measuring plane
max	=	maximum
recycle	=	downstream recycling plane
SI	=	theoretical shock impingement location

Superscripts

inner	=	boundary-layer inner region
outer	=	boundary-layer outer region
$+$	=	dimension in wall units
$*$	=	dimension normalized by δ^*_{ref}
∞	=	freestream value

I. Introduction

THE performance of supersonic engine inlets and external aerodynamic surfaces can be critically affected by shock wave/boundary-layer interactions (SBLIs). Most of these interactions are caused by oblique-shock waves, for which the severe adverse pressure gradients can cause boundary-layer separation. Currently, such problems are avoided primarily through the use of boundary-layer bleed/suction. However, bleed mass flow rates at high Mach numbers can be a large fraction of the engine intake mass flow effect (as much as 10–20%) [1] to achieve the desired control. The loss of mass flow through bleed and the increased inlet requirements are a source of significant performance degradation. This study investigates a novel type of flow control device that may offer similar control benefits without bleed penalties.

Among the multitude of novel flow control methods suggested in recent years, micro vortex generators (μVGs), which are less than the boundary-layer thickness, are particularly interesting because they combine the well-demonstrated capability of vortex generators (VGs) to suppress or delay separation with a significantly reduced device drag [2]. In recent computations performed at the NASA John H. Glenn Research Center at Lewis Field (GRC) (Anderson et al. [3]), it was demonstrated that one particular type of μVG, the microramp, has the ability to produce benefits comparable to traditional boundary-layer bleed while also offering practical advantages such as physical robustness, low cost, and no power requirements. However, there are only a few detailed experimental studies that have examined the impact of these devices on turbulent boundary layers subjected to oblique-shock interactions [4]. Ghosh et al. [5] used hybrid Reynolds-averaged Navier–Stokes with large eddy simulations (RANS/LES) with an immersed boundary method (IBM) to study oblique-shock interactions with microramps. Their RANS/LES approach is helpful in that it allows much higher Reynolds numbers than are practical to compute with an LES. However, the role of the turbulence model empiricism is increased as compared with LES. Their IBM approach is computationally efficient because the grid does not need to conform to the ramps and does not require fine wall-normal spacing on the surface of the ramps. However, their approach yields a wall-function-like description of the microramp boundary layers that may miss some important detailed flow features that would be captured by an LES approach with body-fitted grids.

In this paper, we consider a Mach 3 turbulent boundary layer with a modest Reynolds number to allow an LES approach. In particular, the Reynolds number based on the reference incompressible displacement thickness δ^*_{ref} is about 3800. Note that δ^*_{ref} is the displacement thickness that occurs at the theoretical inviscid shock impingement point x_{SI} for a flat plate with no shocks and no microramps. LES was used to simulate a flat-plate/oblique-shock interaction with and without upstream microramps. Three different microramp configurations are simulated to assess the impact of ramp size and its position on overall performance as measured by total-pressure recovery, boundary-layer growth, and incompressible shape factor of the boundary layer downstream of the interaction.

II. Experimental Methodology

The experiments were conducted in the U.S. Air Force Research Laboratory's (AFRL) Trisonic Gas-Dynamics Facility (TGF) [6] at Wright-Patterson Air Force Base on the forebody boundary-layer management model (see Fig. 1). The TGF is a continuous-circuit tunnel with a 2 ft^2 test section capable of operating in the subsonic, transonic, and supersonic regimes. The model consists of a beveled flat plate with an attached shock generator mounted on a strut so that the plate was located in the center of the tunnel. Figure 1a is a picture of the installed model as viewed through the tunnel schlieren window. Standard boundary-layer transition calculations predicted transition within 20 mm of the leading edge, which is 559 mm upstream of the shock interaction, so no artificial trips were used. As shown in Fig. 1b, the oblique shock generated from the 8 deg shock wedge impinged on the flat plate just upstream of the shock generator sidewall mounts. This configuration eliminated any sidewall separation typical of a grazing wall shock. The boundary layer then propagated downstream to several boundary-layer rakes, where the total pressure of the disturbed boundary layer was measured.

A. Experimental Test Conditions and Microramp

Data were collected at a nominal Reynolds number of 4000 based on the reference displacement thickness δ^*_{ref}. Because δ^*_{ref} was not measured at x_{SI}, its value was obtained from RANS flow simulations.

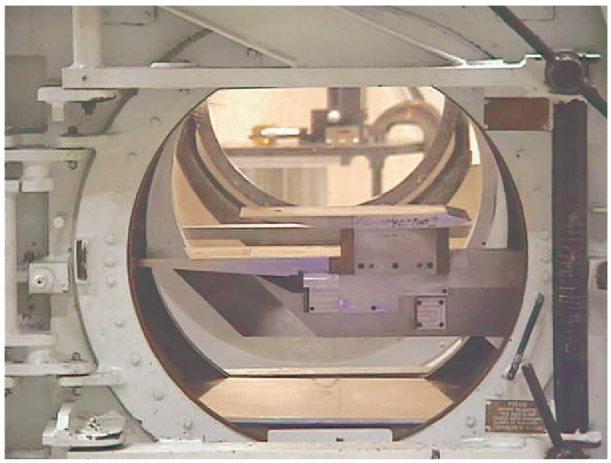

a)

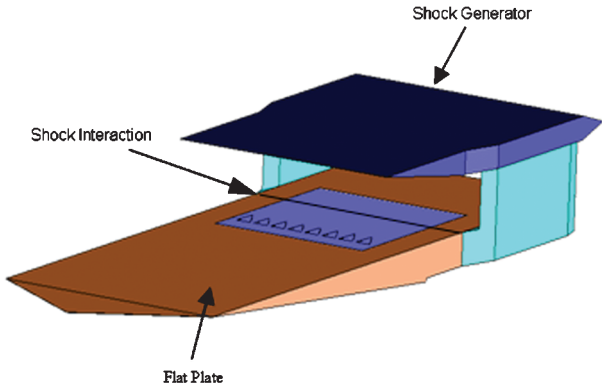

b)

Fig. 1 Experimental setup showing the a) flat plate with shock generator installed in TGF and b) forebody boundary-layer management model schematic.

The Mach number in the test section was nominally 2.98 with a total pressure of 24,000 N/m^2. Tunnel total temperature was maintained at approximately 300 K. Total pressure was held constant throughout the test. The height h of the microramp was 2.82 mm, and the reference displacement thickness δ^*_{ref} was 0.88 mm, so that $h = 3.19\delta^*_{\text{ref}}$. Dimensions of the baseline microramp are shown in Fig. 2. The ramps are a design by Anderson et al. [3], which is based on an investigation of different shapes using RANS simulation. The microramp flow control was machined into a plate that affixed to the base for quick and easy model changes.

B. Instrumentation

Data extraction was based on boundary-layer pitot total-pressure measurements and several static-pressure measurements. The static-pressure rise observed through a shock interaction was only obtained for the baseline oblique-shock cases in which microramps were not present. The model insert plate that contained the flow control devices was replaced with an insert containing an array of static-pressure taps, with the first tap located 88.9 mm upstream of the inviscid shock location. This plate is known as the shock instrumentation plate. Several rows of pressure taps were located in the region of the interaction and extended downstream to the boundary-layer rakes. In addition, there was a static-pressure tap located in front of each boundary-layer rake at the measurement plane. Located 76.2 mm downstream of the inviscid shock location were four boundary-layer rakes that were evenly spaced at 19.05 mm on one side of the centerline. Another one was located on the other side to ensure that the flowfield was symmetric. A total of 12 hypodermic pitot tubes were placed in each rake (see Figs. 3a and 3b). The five lower tubes have a 0.00063 mm outside diameter with a 0.00032 mm inside diameter and the upper seven tubes have outside and inside diameters of 0.00087 and 0.00047 mm, respectively. The two columns of tubes have a lateral separation of 0.0014 mm.

The faces of all the tubes are cut square. The faces of the lower nine tubes are 0.004 mm from the sharp leading edge of the support blade, and for the upper three tubes, this distance is 0.008 mm. The support blade has a leading-edge angle of 40 deg and a width of 0.0025 mm. The pitot-pressure data were reduced to total pressures upstream of the tubes by an iterative solution of the Rayleigh pitot equation. Constant static pressure in the measurement region is based on schlieren images, which showed that the flow after the shock interaction did not contain significant gas dynamic interactions. Rake data and schlieren images for the no-shock case showed a small separation bubble at the base of the boundary-layer rakes. This separation impacted the lower three boundary-layer-rake probes and contaminated the static tap just forward of the boundary-layer rakes. Therefore, the data were reduced to using static tap data from either the most downstream static tap on the shock instrumentation plate, which was 40 mm upstream of the boundary total-pressure-measurement plane, or from a tap added to the microramp flow control plate 5 mm forward of the boundary-layer pitot-pressure measurement plane. The baseline boundary-layer profiles, discarding the lower three probes due to the small separation bubble, fit well to a one-seventh-power profile, indicating a fully developed turbulent boundary layer. The repeatability error was approximately 0.4%, which is very small.

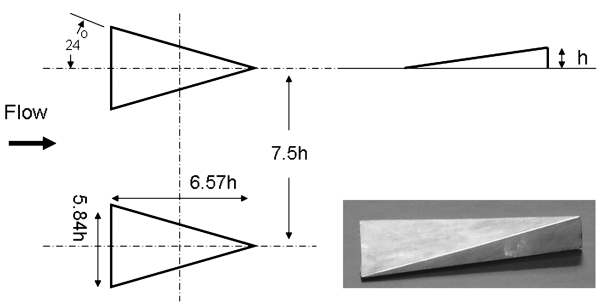

Fig. 2 Dimensions of baseline microramp from Anderson et al. [3].

III. Numerical Methodology

The computational effort consists of large eddy simulations, which provide fine spatial and temporal resolution of the turbulent structures. The WIND code (developed at Arnold Engineering Development Center and NASA GRC and based on the work of Lee et al. [7]) was used to make the LES computations. The LES studies were conducted with and without microramps at flow conditions closely matching those of experiments at AFRL. The moderate Reynolds number of the experimental condition allowed practical LES resolutions and run times.

A. Numerical Schemes and Turbulence Models

A third-order upwind option, combined with a min-mod limiter and a high-resolution structured grid were used to obtain high-fidelity eddy structure and shock interaction simulations. The temporal integration used a second-order, implicit, approximate factorization scheme and Newton subiterations at each time step. The monotone-integrated LES (MILES) approach was selected to capture turbulence effects. The MILES technique is based on Fureby and Grinstein [8], which solves the unfiltered Navier–Stokes equations using high-resolution monotone algorithms. The convection discretization acts as a filter for the nonlinear high-frequency modes to dissipate the kinetic energy accumulated at high wave numbers, thus dispensing the need to use an explicit subgrid-stress modeling. Studies [8] of the forced homogeneous isotropic turbulence showed that the simulated energy spectra depend on the effects of the subgrid-stress model only toward the high-wave-number end of the inertial range and into the viscous subrange. LES becomes independent of the subgrid-stress model if the resolution has a cutoff wave number that lies in the inertial subrange. It has been shown that MILES produces results in close agreement with those obtained by using the Smagorinsky subgrid-stress model [9]. The time step used for the LES study is $\Delta t = \text{CFL}\Delta x/(a^\infty + U^\infty)$, where Δx is the smallest streamwise cell length and a^∞ and U^∞ are the speed of sound and streamwise velocity at the freestream. The Courant-Friedrichs-Lewy (CFL) number was set to 0.4. Several conventional RANS models were examined for comparison [including Spalart–Allmaras and Menter's shear stress transport (SST)], but the differences were not significant. The simple Baldwin–Lomax turbulence model was found to converge rather quickly (and was representative of the other RANS models) and thus is shown for comparison in the below results with a CFL based on the streamwise cell length of 0.8. However, comparison among all three turbulence models will also be shown for a sample case with a baseline microramp and a shock interaction.

B. Rescaling–Recycling Method

The rescaling–recycling method, originally developed by Lund et al. [10] for incompressible flows, has been extended for compressible boundary-layer flows by Urbin et al. [9,11]. The result is a computationally efficient method of generating turbulent inflow condition by eliminating the need to simulate boundary-layer flows from the leading edge of the flat plate, through transition. For the recycling method, the instantaneous flowfield at a given downstream location is rescaled using boundary-layer theory to match the average flowfield at an upstream recycle location, where it can then be used as an input for another cycle. The downstream plane will be denoted as the recycle plane and the upstream plane will be denoted as the inlet plane. This technique requires that the distance between the two recycling stations is sufficiently long (i.e., x^+ of 1000 wall units [11]). The normalized fluid convection time scale based on the freestream velocity at the recycling zone is $t^* = 0.095$, where $t^* = t_{\text{recycle}}/\tau_{\text{dom}}$, and t_{recycle} is the fluid convection time scale within the recycling zone defined as $L_{\text{recycle}}/U_\infty$, where L_{recycle} is the streamwise length of the recycling zone. Likewise, τ_{dom} is the time scale for the flow to convect through the entire domain defined as L/U_∞, where L is the streamwise length of the domain. The Lagrangian integral time scale of a turbulent eddy τ_{eddy} in a boundary layer can be computed using the following equation [12]:

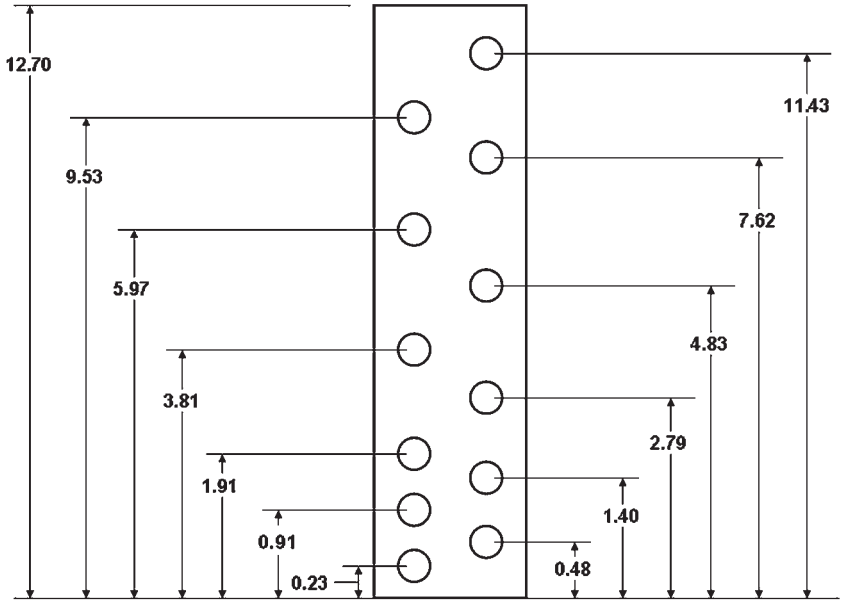

a)

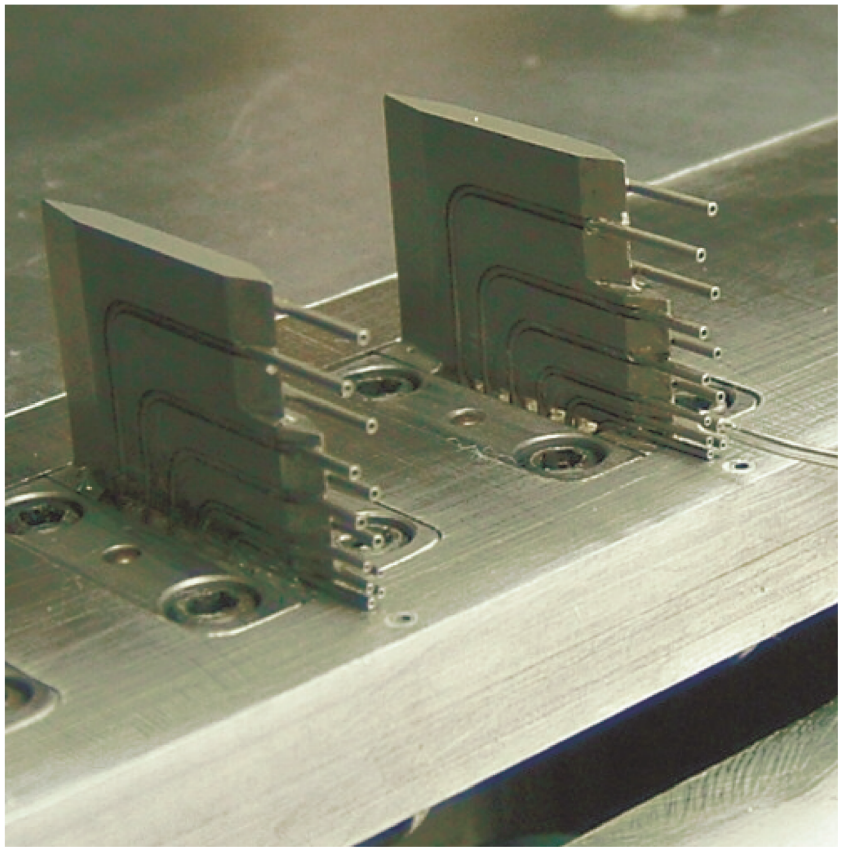

b)

Fig. 3 Boundary-layer rakes: a) schematic in which holes represent pitot probe positions (mm unit) and b) actual picture of the rakes.

$$\tau_{\text{eddy}} = \min[\upsilon_w(10 + 0.4y^+)/U_\tau^2, 0.2\delta/U_\tau] \tag{1}$$

where υ_w is the kinematic viscosity at the wall, y^+ is the normal distance in wall units, and U_τ is the frictional velocity. Normalizing the result using the above equation with τ_{dom}, then τ^*_{eddy} approximately ranges from 0.021 to 0.037, which is at least 2.5 times smaller than that of the fluid convection time scale. Note that the actual convection speeds of the turbulent eddies are far less than the freestream velocity. Therefore, the periodic forcing frequency should be sufficiently large enough for separated flows for which the frequencies have strong correlations with the low-speed eddies. Multilayer scaling [13] can be used for the boundary-layer profile, and we decompose it into an inner and outer layer, similar to Urbin et al. [9,11]. The time- and spanwise average streamwise velocity U can be used to obtain the frictional velocity at the wall from which the inner-layer velocity profile U^{inner} can be described in terms of the law of the wall:

$$U = \frac{1}{\tau_f D}\int_0^D \int_0^{\tau_f} u \, \mathrm{d}t \, \mathrm{d}z \tag{2}$$

$$U^{\text{inner}} = U_\tau(x)\left[\frac{1}{\kappa}\ln(y^+) + C\right] \tag{3}$$

In the first expression, u is the instantaneous streamwise velocity, D is the width of the domain, and τ_f is the total integration time required for convergence. In the second expression, κ is the von Kármán constant, and C is an empirical constant. Since U_τ is assumed to be only a function of the streamwise coordinate x, the average streamwise velocity at the inlet station can be obtained by multiplying the frictional velocity ratio β:

$$U^{\text{inner}}_{\text{inlet}} = \beta U^{\text{inner}}_{\text{recycle}}(y^+_{\text{inlet}}) \tag{4}$$

where $\beta = U_{\tau,\text{inlet}}/U_{\tau,\text{recycle}}$. Note that $U^{\text{inner}}_{\text{recycle}}$ has been interpolated to the y^+ coordinate system at the inlet station. The outer layer follows the velocity defect law such that the following similarity rule can be applied:

$$U^\infty - U^{\text{outer}} = U_\tau(x) f(\eta) \tag{5}$$

where $\eta = y/\delta$ and δ is the boundary-layer thickness. Similarly, the outer layer of U at the inlet station can be obtained by

$$U^{\text{outer}}_{\text{inlet}} = \beta U^{\text{outer}}_{\text{recycle}}(\eta_{\text{inlet}}) + (1-\beta)U^\infty \tag{6}$$

where $U^{\text{outer}}_{\text{recycle}}$ is interpolated to the η coordinate system at the inlet station. As for the fluctuation velocity, $u' = u - U$, where u is the instantaneous streamwise velocity, the rescaled fluctuation the velocities for the inner and the outer layer are obtained from the following equations:

$$u'^{\text{inner}}_{\text{inlet}} = \beta u'^{\text{inner}}_{\text{recycle}}(y^+_{\text{inlet}}, z, t) \tag{7}$$

$$u'^{\text{outer}}_{\text{inlet}} = \beta u'^{\text{outer}}_{\text{recycle}}(\eta_{\text{inlet}}, z, t) \tag{8}$$

The composite equation is then obtained by combining the inner and outer regions of the boundary-layer profile using a weighting function:

$$u_{\text{inlet}} = \beta(U^{\text{inner}}_{\text{recycle}} + u'^{\text{inner}}_{\text{recycle}})[1 - W(\eta_{\text{inlet}})] + \beta(U^{\text{outer}}_{\text{recycle}} + u'^{\text{outer}}_{\text{recycle}})W(\eta_{\text{inlet}}) \tag{9}$$

where the weighting function [9] is defined as

$$W(\eta) = \frac{1}{2}\left[1 + \tanh\left(\frac{4(\eta - 0.2)}{0.6\eta + 0.2}\right)\Big/\tanh(4)\right] \tag{10}$$

Rescaling the wall normal (transverse) velocity v and the temperature T involves similar procedures, except for setting $\beta = 1$: β is set to the same value as the u case for spanwise velocity w. The pressure at the inlet is assumed to be constant due to negligible fluctuations [13]. Thus, the density field at the inlet station can be computed directly from the rescaled temperature. Note that the above method slightly differs from that of Urbin et al. [9,11] with respect to Eqs. (4) and (6). Van Driest transformation applied to the mean streamwise velocity profile [9,11] requires a priori knowledge of the mean profile, which is difficult to obtain for the present low-Reynolds-number case. On the other hand, eliminating the transformation allows β to be factored out in Eq. (9), such that the instantaneous velocity profile at the recycling plane can be used directly. Xu and Martin [14] have shown that even a pure periodic coupling between the inlet and the recycling plane yields good agreement with the rescaling–recycling results similar to that of Urbin et al. [9,11]; thus, the present method was deemed appropriate.

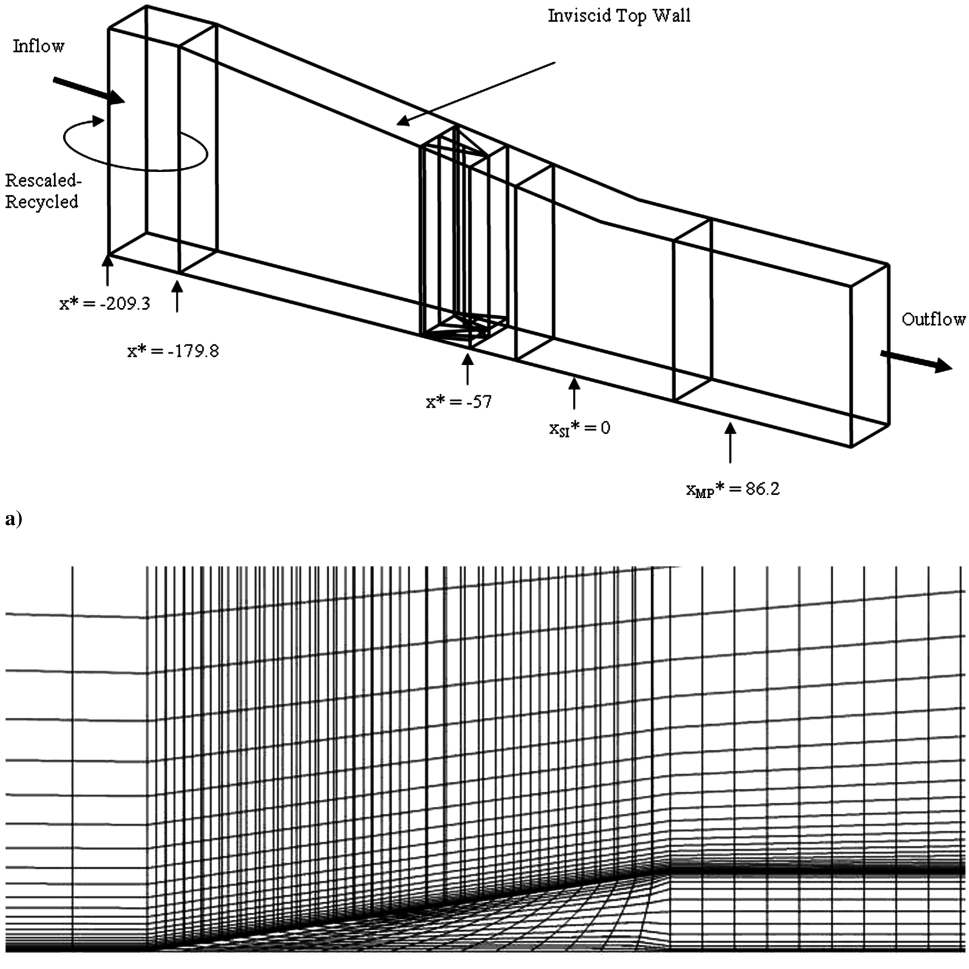

Fig. 4 Grid topology for a) angled view of the whole domain and b) zoom-in at the microramp.

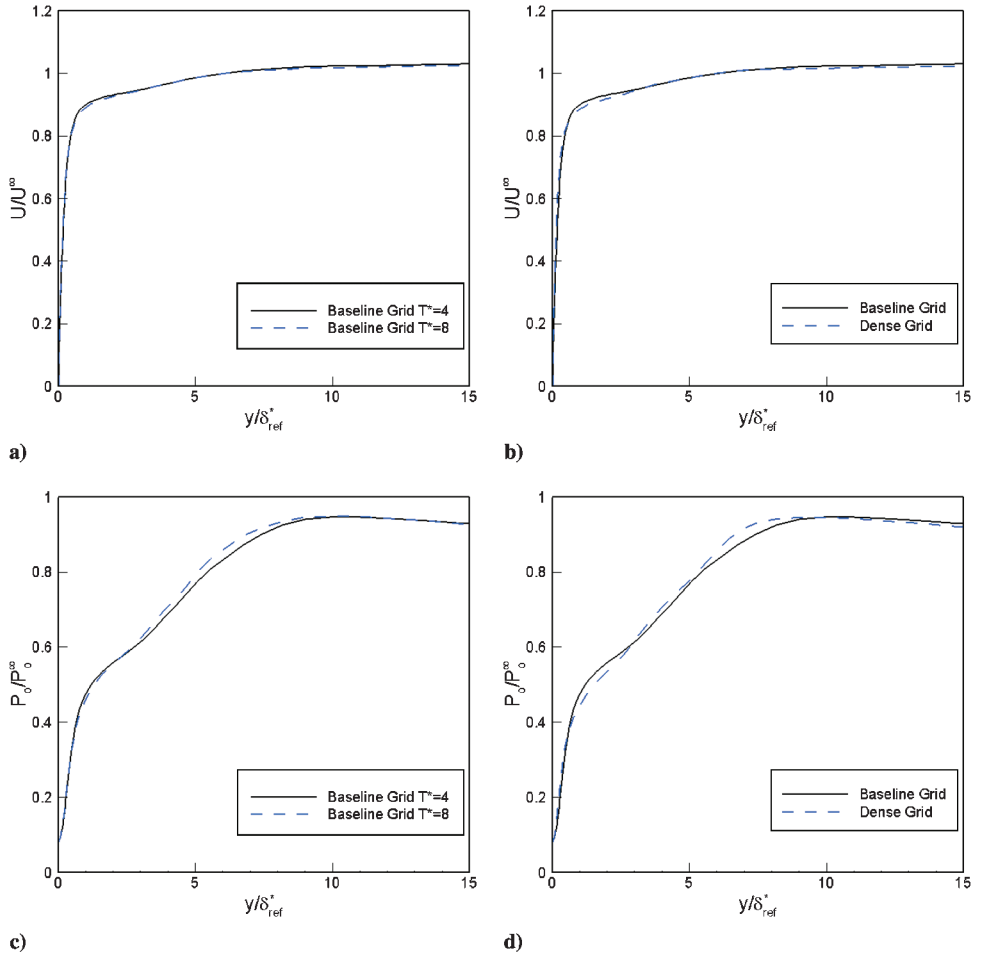

Fig. 5 Study of a) integral time convergence on the velocity profile, b) grid resolution on the velocity profile, c) integral time convergence on the total-pressure profile, and d) grid resolution on the total-pressure profile for the baseline ramp.

In this study, the initial solution in the recycling domain is based on a RANS mean velocity profile that corresponds to the desired inlet boundary-layer thickness. It was found that using inviscid sidewall (instead of spanwise periodic) boundary conditions allowed the instabilities to develop faster. Therefore, the recycling was initially implemented with inviscid sidewalls for several flow convection sweeps. Then spanwise periodic conditions were used until the inflow became statistically stationary with the proper boundary-layer thickness. To rescale the flowfield at the recycle station to the inlet station coordinates y^+_{inlet} and η_{inlet}, the boundary-layer-thickness ratio and the frictional velocity ratio must be computed a priori. These values can be estimated from empirical relations given by Smits and Dussauge [15] for the inner-region rescaling:

$$\frac{U_{\tau,\text{inlet}}}{U_{\tau,\text{recycle}}} = \left(\frac{\delta_{\text{recycle}}}{\delta_{\text{inlet}}}\right)^{\frac{1}{10}} \tag{11}$$

The outer-region rescaling method was not found to be generally robust for changes in Mach number and Reynolds number, so a different technique was employed. Specifically, a feedback loop was instituted to prescribe the scaling used for recycling to ensure that the final boundary-layer-thickness ratio converged to the initial ratio:

$$\frac{\delta_{\text{recycle}}}{\delta_{\text{inlet}}} = \frac{\delta_{i,\text{recycle}} + \frac{1}{2}(\delta_{\text{current,inlet}} - \delta_{i,\text{inlet}})}{\delta_{i,\text{inlet}}} \tag{12}$$

where $\delta_{i,\text{inlet}}$ and $\delta_{i,\text{recycle}}$ are the desired values for the displacement thickness at each station, based on RANS. The U profile at the inlet station is updated at each iteration so that $\delta_{\text{current,inlet}}$ can be directly computed. The flowfield stabilizes to the targeted $\delta_{i,\text{inlet}}$ at the inlet station as the U profile converges, and the ratio of δs in Eq. (10) becomes a constant.

C. Computational Domain

As shown in Fig. 4a, the computational domain consists of 11 zones. The zones are required to grid the complex geometry of the microramp and an oblique-shock wedge of angle γ. The dimensions of the domain are based on the height h of the microramp and the reference displacement thickness δ^*_{ref}, yielding a ratio of 3.19, which is the same as the experiment. The geometry of the microramp is shown in Fig. 2 and is defined to be the baseline microramp configuration. The computational domain, shown in Fig. 4, is a scaled version of the test section (Fig. 1) of the wind tunnel at the AFRL. The length of the domain is $312\delta^*_{\text{ref}}$ (11,052 in wall units) and the width of the domain is $23.7\delta^*_{\text{ref}}$ (840 in wall units), where the

Table 1 Dimensions of the domain and the μVGs

Parameters	NR	BR	HR	HRHD
L^*	312	312	312	312
L^+	11,052	11,052	11,052	11,052
D^*	23.7	23.7	23.7	23.7
D^+	840	840	840	840
E^*_{inlet}	86.3	86.3	86.3	86.3
E^+_{inlet}	3,055	3,055	3,055	3,055
E^*_{exit}	61.1	61.1	61.1	61.1
E^+_{exit}	2,164	2,164	2,164	2,164
h^*	No device	3.19	1.59	1.59
h^+	No device	112	56	56
c^*	No device	20.95	10.48	10.48
c^+	No device	736	368	368
d^*	No device	18.63	9.32	9.32
d^+	No device	654	327	327
s^*	No device	23.93	11.97	11.97
s^+	No device	840	420	420

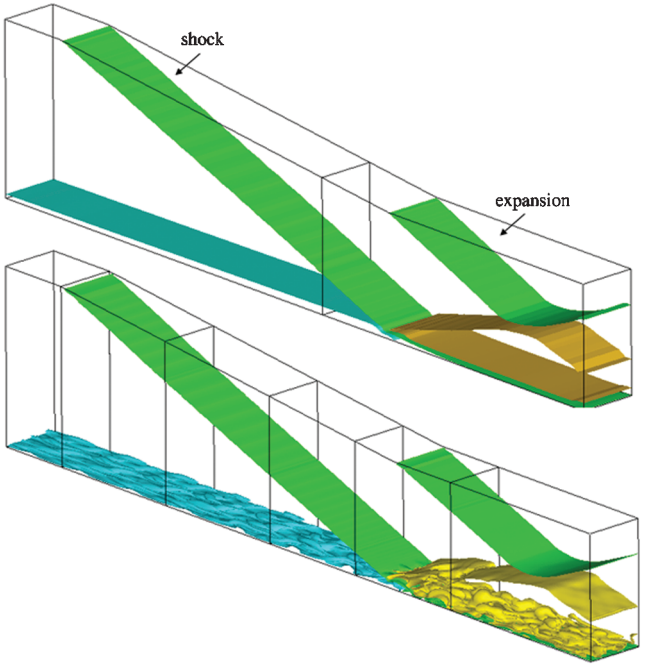

Fig. 6 Isosurface of density for NR with RANS (top) and LES (bottom).

spanwise coordinate z is defined as 0 at the centerline of the computational domain. The height varies from $86.3\delta^*_{\text{ref}}$ to $61.1\delta^*_{\text{ref}}$ (3055 to 2164 in wall units) at the entrance and the exit of the domain. The streamwise distance was normalized by the displacement thickness and centered at the theoretical shock impingement location as $x^* = (x - x_{\text{SI}})/\delta^*_{\text{ref}}$. The microramp trailing edge is located at $x^* = -57$, which is upstream of the shock impingement location. The first zone (recycling zone), for which the length is $29.5\delta^*_{\text{ref}}$, generates turbulent boundary-layer inflow conditions using the rescaling–recycling method. The supersonic flow enters into the test section, in which the wedge ($\gamma = 8$ deg) is placed at the top ceiling, generating a 25.6 deg shock wave. The measuring plane x_{MP} is located at $x^* = 86.2$, which corresponds to the location of the pitot probes in the experiment, as shown in Fig. 4a. The no-slip condition is imposed on the bottom plate and the microramp, whereas the top ceiling has inviscid wall conditions. Periodic boundary conditions are imposed on the side walls to represent arrays of microramps in the spanwise direction, similar to the experimental configuration. The first grid point normal to the bottom wall is at $y^+ = 0.8$ throughout the domain, based on the shear stress at the inlet station of rescale–recycle zone, where the skin friction is approximately 1.46×10^{-3}. The streamwise and the spanwise grid spacing correspond to x^+ of 28 and z^+ of 13, yielding a total of 3.2 million nodes for the entire domain. The grid resolution is higher at the microramp to capture the fine vortical structures, as shown in Fig. 4b.

D. Spatial Independence and Time Integration Study

A grid resolution study was performed by increasing grid points of the baseline grid by 30% for each of the computational coordinate directions (ξ, ψ, and z), resulting in an increase of 2.2 times the total number of nodes. This was defined as the dense grid, which maintained the same grid aspect ratios and distribution patterns as that of the baseline grid. The results were time-averaged after the initial transients had convected out of the computational domain. The average of a given variable ϕ is defined as

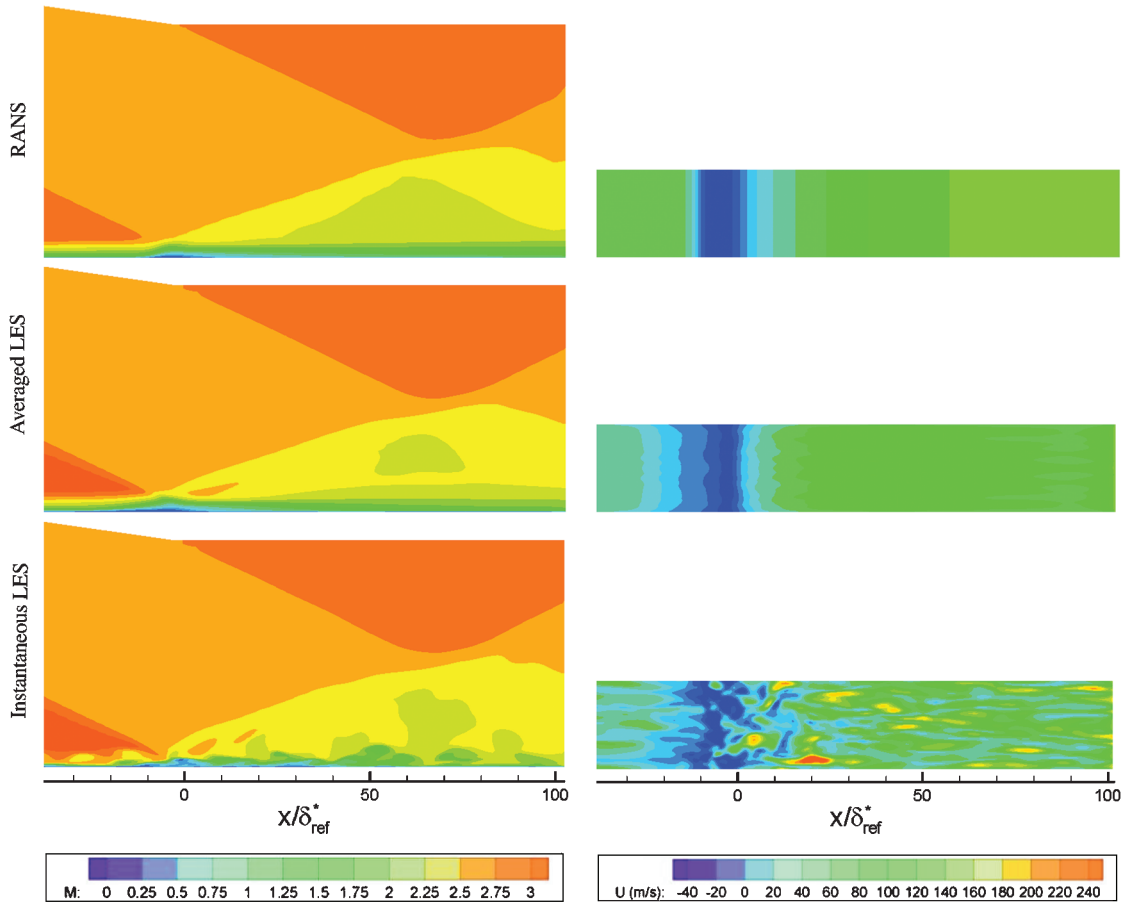

a) Streamwise view of z* = 0 plane **b) Spanwise view of y+ = 1 plane**

Fig. 7 Visualization of various plane for NR $z^* = 0$ and at $y^+ = 1$ from $x^* = -38$ to $+102$: a) midspan Mach number contours for $y^* = 0$ to 69 and b) near-wall streamwise velocity contours for $z^* = -11.9$ to $+11.9$. Note that the plane $y^+ = 1$ corresponds to the first vertical grid point above the wall, which was the same for all flows, since this grid point was based on the NR shear stress at $x^* = -209.3$.

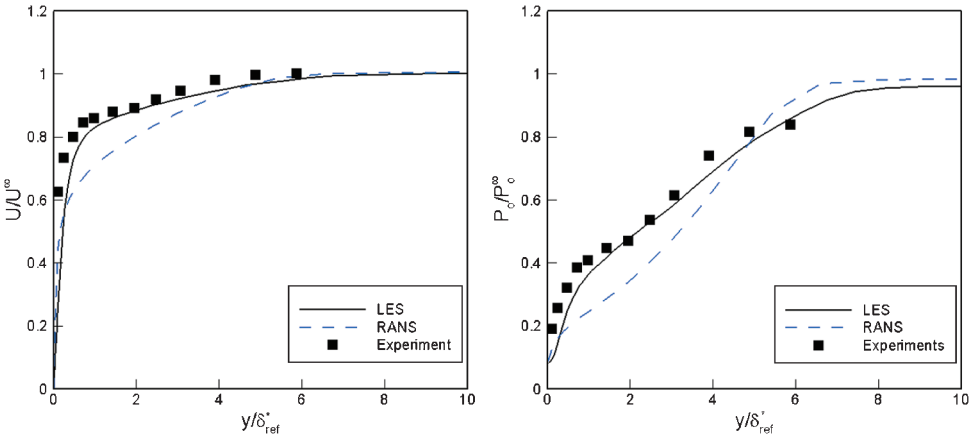

Fig. 8 Streamwise velocity and total-pressure profile comparison between RANS, LES, and experimental data for NR at measuring plane ($x^*_{MP} = 86.2$).

$$\bar{\phi} = \frac{1}{\tau_{\text{int}}} \int_{t}^{t+\tau_{\text{int}}} \phi \, \mathrm{d}t \tag{13}$$

where τ_{int} is the total integration time. This quantity can be normalized as $\tau^* = \tau_{\text{int}}/\tau_{\text{dom}}$. A convergence study of time integration used for averaging was conducted by comparing results from integration time of $\tau^* = 4$ and 8, as shown in Figs. 5a and 5c. The average error of the two mean velocity profiles (Fig. 5a) was 0.7%, which shows good statistical convergence even at $\tau^* = 4$. The average velocity profiles and the average total-pressure profiles (where P_o^∞ is the freestream total pressure before the shock) were compared between the solutions from these two grids and the results are quite similar, as shown in Figs. 5b and 5d, yielding an average error of 0.3% for two mean velocities. The differences are amplified in the total-pressure profiles, since P_o/P is strongly sensitive to Mach number changes (e.g., the proportionality approaches M^7 for high-Mach-number conditions). The grid resolution effects were considered small enough so that the baseline condition was deemed appropriate to obtain predictions between different microramp configurations. Thus, the remaining computations were performed with the baseline grid with the integration time of $\tau^* = 4$.

IV. Results

We present experiments and simulations of Mach 3 turbulent boundary layers with Re_{ref} of 3800 (based on δ^*_{ref}), where the freestream pressure and the temperature are 7076 N/m^2 and 582.3 K, respectively. A scaled version of the AFRL test section, shown in Fig. 4, is used for the computational domain. For the given conditions, a turbulent flow solution was obtained for a clean plate (i.e., no ramps and no shock; abbreviated to NR) as well as for a shock and the baseline microramp (BR) configuration. Microramps with one-half of the overall size (HR) and with one-half of the distance to the shock interaction (HRHD) were also simulated to study the effects of ramp height and location on displacement thickness, total-pressure loss, and shape factor. The dimensions of the simulated cases are summarized in Table 1, and the definitions of the length, width, and height of the computational domain and the device are in the Nomenclature.

A. SBLI with No Microramp

The supersonic boundary-layer flow with the oblique shock but with no microramp (NR) was first studied to understand the flow characteristics, such as shock impingement and boundary-layer separation characteristics. Density isosurface of RANS and instantaneous LES for the shock wave interacting with the turbulent boundary layer are shown in Fig. 6. Both techniques indicate a reflected shock, but the LES predictions show the presence of turbulent structures in the boundary layer, which are significantly altered as they pass through the shock. In particular, the aspect ratio of turbulent structures was changed, as they tend to have greater

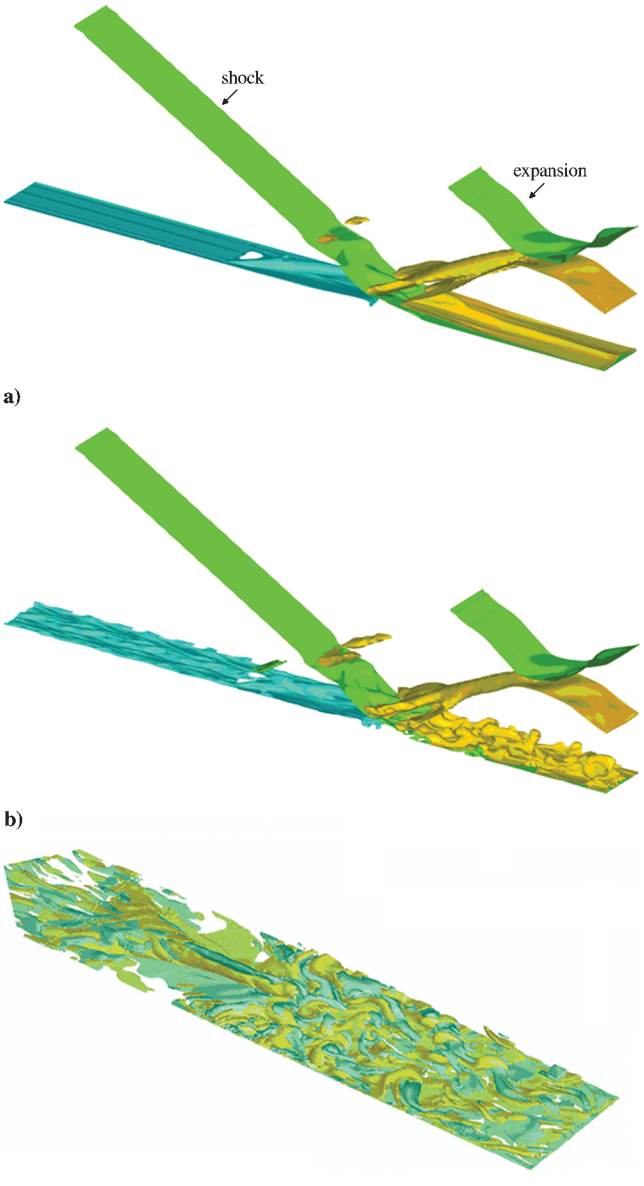

Fig. 9 Isosurface of a) density for averaged LES, b) instantaneous LES, and c) streamwise vorticity of instantaneous LES.

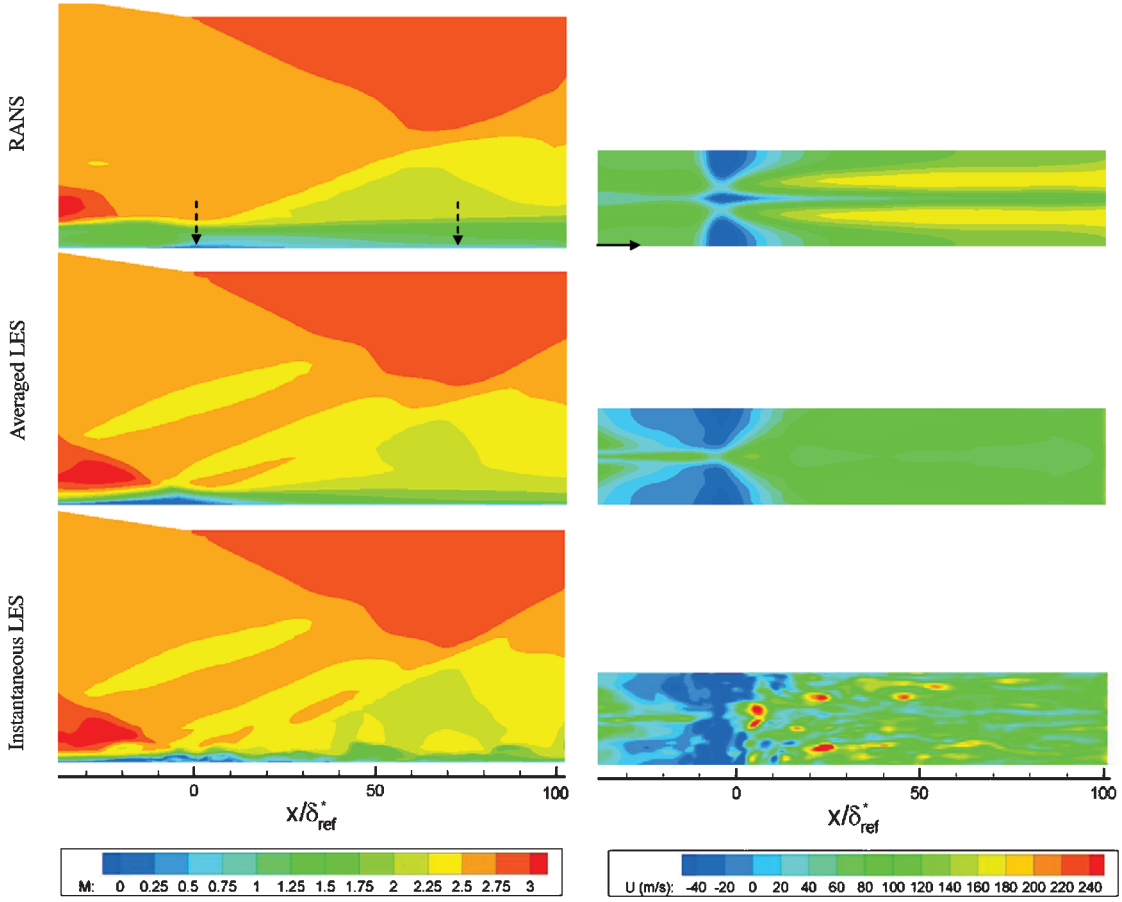

a) Streamwise view of z* = 11.9 plane b) Spanwise view of y^+ = 1 plane

Fig. 10 Visualization of a) streamwise and b) spanwise planes for BR with same contours and domain as for Fig. 7. The solid arrow indicates the spanwise location of the streamwise contours, and the two dashed arrows indicate the two streamwise positions shown in Fig. 11.

height and shorter streamwise length. The former may be attributed, in part, to the boundary-layer thickening, and the latter may be attributed to the shock unsteadiness [16]. The structures begin to relax toward the preshock aspect ratios further downstream.

Figure 7 shows streamwise views of the Mach number contours and spanwise views of the velocity contours for RANS, averaged LES, and instantaneous LES. As seen in the streamwise view, which begins at $x^* = -57$, the primary shock impinges on the turbulent boundary layer and reflects into the upper region (where it collides with the upper-wall expansion wave, causing both of the waves to reflect once more as they exit the outflow plane at $x^* = 102$). The spanwise and streamwise views reveal that the average LES results show a larger flow separation than the RANS results. The larger separation height creates an expansion wave posterior of the separation-bubble peak for the averaged LES case. Compared with RANS, the flow separation for the averaged LES is also more gradual and initiates further upstream of the inviscid shock location ($x^*_{SI} = 0$). This effect is attributed to the appearance of many separation cells in the instantaneous case; that is, there are many streaks of flow separation that occur upstream and even downstream of the primary region of separation. These separated cells may also be responsible for the change in the turbulent structures just after the shock, as noted in Fig. 6. Further downstream, entrainment of high-speed fluid in the instantaneous LES is indicated by yellow streaks that drive the recovery of the boundary layer.

The numerical predictions and measurements of the velocity and the total-pressure profiles at the measurement plane ($x^*_{MP} = 86.2$) are shown in Fig. 8. The results are normalized with the freestream velocity and the total pressure. The results indicate that the LES results gave closer agreement with experimental data than the RANS results. In particular, the velocity shape for LES is fuller than RANS, indicating that the latter underpredicts boundary-layer recovery, despite predicting a small separation region. The poor predictions of the RANS result may be partially attributed to the empiricism associated with turbulence modeling. However, it should be noted that RANS turbulence models are more suited and have been calibrated to predict flows at higher Reynolds number [17]. In fact, the predicted RANS profiles are similar to the subsonic equilibrium boundary-layer profiles measured by Mellor and Gibson [18], in which the two distinct slopes exist for the inner and outer regions. The discrepancies between the LES result and the experiment begin to grow, yielding different velocity gradients near the wall. Experimental uncertainties could be the primary reason that the data acquisition near the wall becomes more difficult. However, the Reynolds number effect are not expected to play a significant role for the flow separation process, since the difference in their Reynolds numbers are relatively small ($Re_{\theta,LES} = 2350$ and $Re_{\theta,EXP} = 2500$, where the momentum thickness θ is measured at x_{SI}). The predictions of downstream total pressure are also shown in Fig. 8. The total-pressure curve for RANS undershoots for y locations less than $5\delta^*_{ref}$

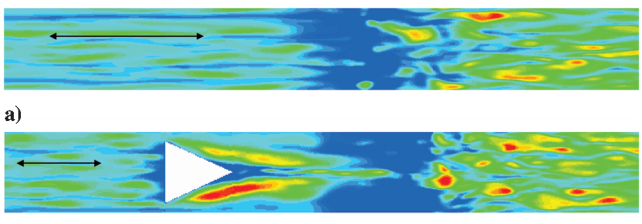

Fig. 11 Velocity contours at $y^+ = 5$ showing streamwise lengths of 8δ (400 wall units) and 20δ (1000 wall units) in the spanwise length for a) NR and b) BR.

but overshoots for higher heights of $6\delta^*_{ref}$ compared with the experimental data, where the bottom wall is at $y = 0$. The LES predictions are significantly better than those for the RANS but indicate higher discrepancies with the total pressure, which is consistent with the increased sensitivity to Mach number.

B. Effects on SBLI with Baseline Microramp

The BR inserted into the above SBLI was investigated experimentally and computationally. Figure 9 shows that the microramp causes a small shock wave that interacts weakly with the primary downward oblique shock. More important, as the flow travels over the microramp, a vortex tube (mostly consisting of a pair of primary counter-rotating vortices) is generated. This vortex tube initially rises due to the flow separation region but then descends closer to the wall after the reflected shock. During this process, it loses its coherency, as shown in the averaged LES isosurfaces (Fig. 9a). However, it interacts with the vorticity of the turbulent structures downstream of the reflected shock, as shown in the instantaneous LES isosurfaces (Fig. 9b). It can be seen that the shock interaction weakens the vortex-tube cohesion vorticity significantly compared with that of the turbulent structures (Fig. 9c). However, these streamwise vortices are associated with the recovery of the turbulent structures to preshock characteristics. A streamwise view of the Mach number contours located at the middle of two periodic microramps ($z^* = 11.9$ and z/δ^*_{ref}) is shown in Fig. 10. This spanwise location was chosen because it is the point where the flow separation is largest. A spanwise view is also shown in this figure for the velocity field just above the wall ($y^+ = 1$). In general, the RANS and LES predictions yield fundamentally different results. The RANS boundary layer at this spanwise location is generally thick both during and after the SBLI, but the separation region is quite thin. In contrast, the LES boundary layer is thinner but includes a larger separation region, followed by a local expansion fan. In the spanwise view, it can be seen that this separation region also extends further upstream. This is consistent with the NR results, where the RANS flow predicted less impact of the SBLI and predicted a slower recovery downstream compared with the LES flow. In the spanwise view for the LES predictions, the strong streamwise vorticity generated by the microramp creates an attached flow region downstream of the microramp centerline. The RANS predictions yield an additional flow separation segment at the center, which is due to the vortex-tube pair traveling at a higher height (thick boundary layer), such that the secondary vortices are developed under the primary pair at the shock impingement region.

Compared with the NR LES results, the boundary layer with the BR is thicker near the interaction with a larger separation and is somewhat thinner near the end of the computational domain. At the downstream location, the spanwise instantaneous contours tend to show more high-speed streaks, indicating entrainment from the upper region of the boundary layer, which is attributed to the microramp streamwise vortices.

Low- and high-speed strips for which the streamwise lengths are approximately 8δ to 20δ have been found upstream of the oblique shock in various samples of instantaneous flow solutions, similar to the results in Ganapathisubramani et al. [19]. These structures may contribute to the undulations of the shock position and are substantially changed downstream of the shock interaction to be shorter in length and more volatile, owing to the reattachment of a strongly turbulent free shear layer, as can be seen in Fig. 11a. However, by placing a flow control device, the character of the structures downstream of the shock show an even larger increase in the number of high-speed strengths, which implied improved mixing due to the production of streamwise vorticity (Fig. 11b).

Mach number contours from RANS and LES close to the inviscid shock location ($x^* = -3.7$) are shown in Fig. 12, in which the two counter-rotating vortices generated from the microramps have moved close to each other and have begun to move upward away from the wall. While the circular tube structure is retained for the instantaneous LES, the unsteadiness of the boundary layer increases due to the shock interaction. Just to the side of this vortex pair, the boundary-layer thickness is reduced because high-speed fluid is entrained downward. However, near the spanwise edges of the domain, the boundary layer is thicker as the vortex pair impact is lessened. These trends are less evident in the RANS results as compared with the averaged LES results. As the flow convects downstream of the shock, the vortex structure gradually diffuses until only the wake of the microramp remains at the measuring plane shown in RANS and averaged LES results. In the instantaneous LES contours, it can seen that the vortex pair size is larger and stronger than the turbulent structures at $x^* = -3.7$ but is much less pronounced at $x^* = 86$.

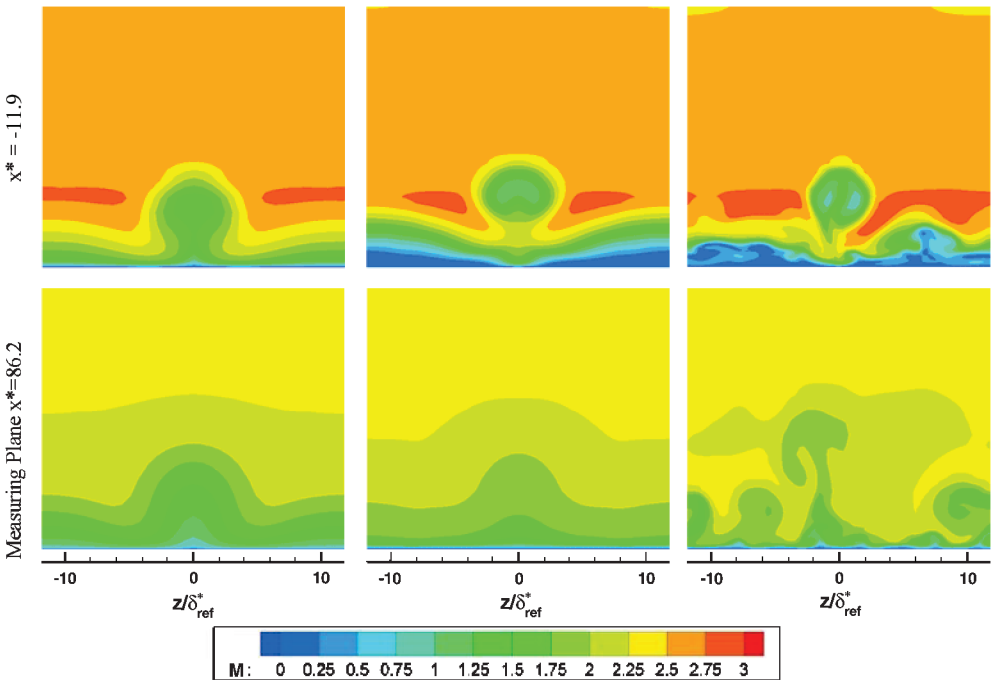

Fig. 12 Visualization of cross-sectional plane Mach contours for BR at $x^* = -11.9$ (near shock impingement) and $x^* = 86.2$ (measuring plane) for a) RANS, b) averaged LES, and c) and instantaneous LES.

The velocity profiles are shown in Fig. 13 for each rake location. Rake 1 is located at $z^* = 11.85$ from the center of the domain (middle of two microramps) and rake 2 is at $z^* = 9.7$, which is at the tip of the leading edge. Rake 3 position is at $z^* = 7.5$. Similar to the NR configuration, the streamwise velocity profiles from the averaged LES results have closer agreement with the experimental data than the RANS results, consistent with NR results (Fig. 8). The LES predictions of the velocity profiles also indicate a much fuller boundary layer near the exit of the computational domain as compared with the RANS results, which is consistent with the contours shown in Fig. 10. The total-pressure profiles indicate larger differences between the LES results and the measurements, which are attributed to the higher sensitivity of this variable to Mach number changes.

As mentioned earlier, a study was conducted to see if the RANS results were specific to a specific turbulence model, especially because the RANS results substantially underpredicted the velocity and total-pressure profiles. Two additional RANS turbulence model were investigated: SST κ-ω and Spalart–Allmaras. The comparisons are shown in Fig. 14, in which all three models yield similar underpredictions, indicting that the conventional RANS approach is not likely to be successful for this flowfield, due to the combination of strong shock-induced separation and modest Reynolds number. Such a result is consistent for other separated flows at high-Mach-number flows [20,21]. Therefore, only LES predictions will only be shown for the remaining flowfields.

C. Effects of Microramp Size and Location (HR and HRHD)

To study the effects of microramp size and location, two additional configurations were investigated and compared with the BR configuration. To investigate size effects, a 50% smaller microramp was placed at the same location as the BR configuration; this configuration is denoted as HR. To simultaneously investigate ramp location effects, a 50% smaller microramp was located with its trailing edge (apex) at the midpoint between the BR trailing edge and

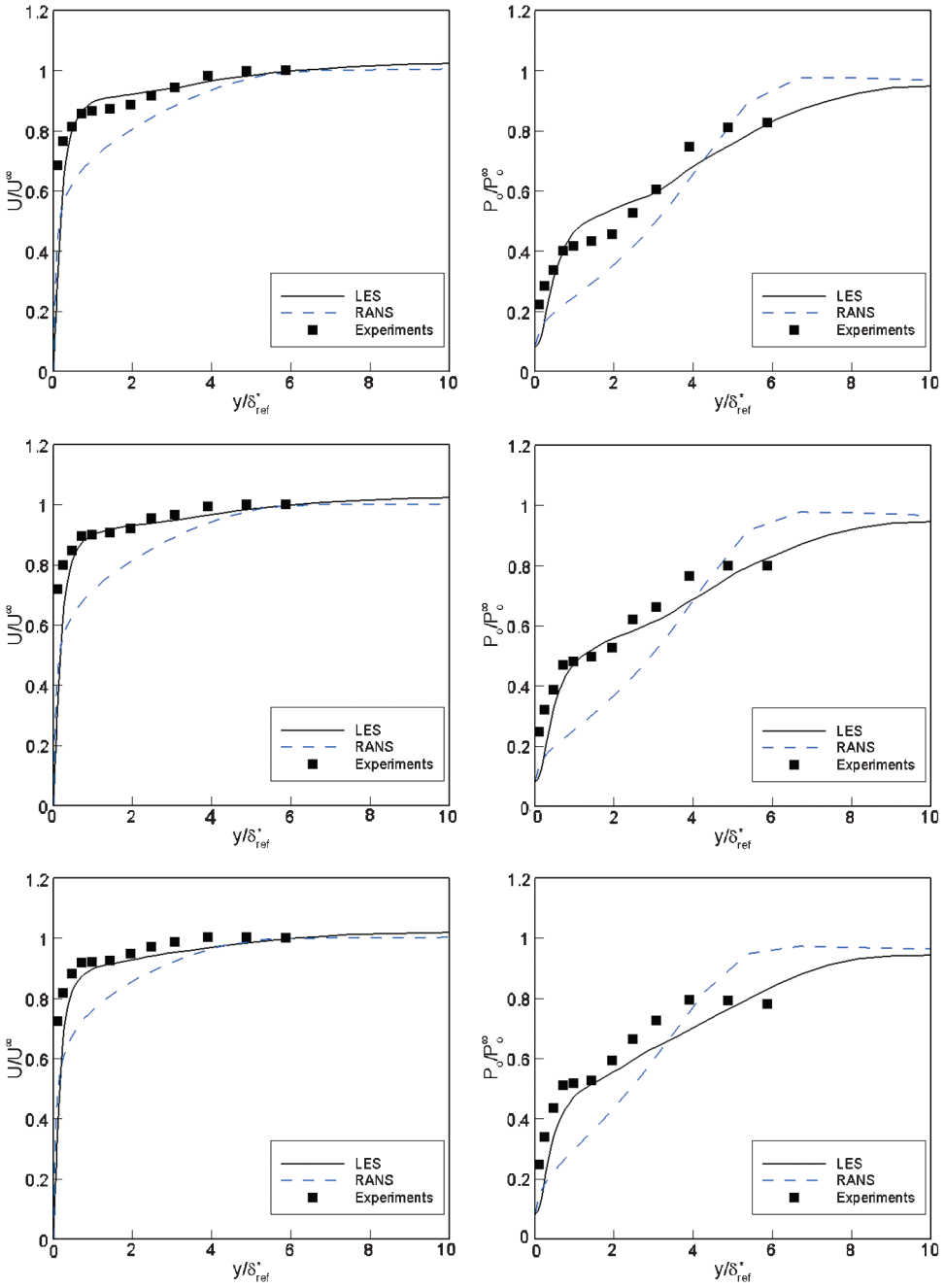

Fig. 13 Comparison of streamwise velocity and total-pressure profile for LES, RANS, and experimental data for BR at $x^* = 86.2$ (measuring plane) for rake 1 (top, $z^* = 11.8$), rake 2 (middle, $z^* = 9.7$), and rake 3 (bottom, $z^* = 7.5$).

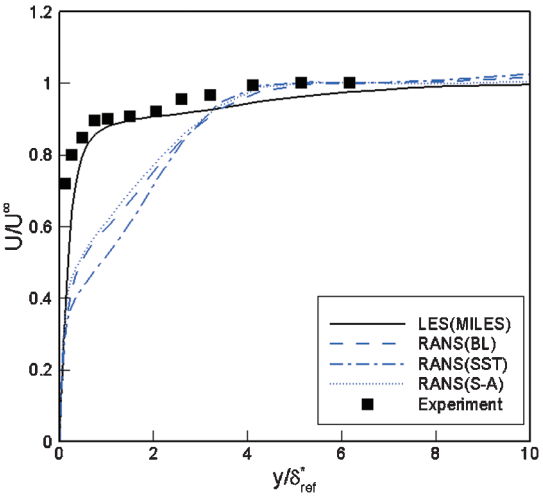

Fig. 14 RANS turbulence model comparison.

the shock impingement locations. This case is denoted as HRHD and this choice is consistent with measurements by Pitt Ford and Babinsky [22], who noted that the longevity and impact of the streamwise vorticity scaled primarily with the ramp height. Both the HR and HRHD configurations retained the same spanwise spacing ratio (width normalized by height) as BR. Since these cases employed the same physical domain as that for the BR case, a consistent spacing ratio yielded two smaller side-by-side ramps in the computational domain (as compared with a single larger ramp for the baseline case).

Figure 15 compares the near-wall average and instantaneous spanwise velocity contours for the two new configurations with the baseline-ramp results. The instantaneous LES contours show that the shock interaction regions again include many pockets of separated flow (rather a single large separation region), and that the streamwise vorticity downstream of the microramps tends to eliminate even instantaneous pockets of separated flow. The averaged LES results show that the separated areas have generally decreased for the HR and HRHD configurations in comparison to the baseline microramp configuration. This reduction in separation can be attributed to the closer proximity of the microramp to the shock interaction and is most evident for the HRHD configuration. (The effects of the streamwise vortices are evident just upstream of the interaction.) In contrast, the HR has a separated flow region downstream of the ramp on the ramp centerline. These separated regions indicate that the microramp vortices from this configuration may be too weak. This interpretation is consistent with the expected reduced vortex strength at a fixed downstream location as the device height is reduced [2,22,23]. The reduced scaling of the microramp resulted in a higher spanwise frequency, which helped reduce the overall separated area. The HR and HRHD configurations also produce more high-speed streaks (Fig. 15) compared with the BR, indicating improved flow recovery.

The instantaneous LES cross-sectional Mach number contours just downstream of the microramps and at the measurement stations for the BR, HR, and HRHD configurations are shown in Fig. 16 along with the averaged flow solution. The instantaneous LES at the trailing edge for HR and HRHD are consistent with a factor-of-2 reduction in the width and height of the counter-rotating vortex pairs compared with the BR configuration. At the measurement plane, the vortex pairs are more evident for the BR, an indication that they are less dissipated. The reduced dissipation is attributed to the increased distance away from the strong near-wall turbulence as well as their increased strength. This trend is also evident in the averaged Mach contours, where the BR configuration shows a more prominent wake deficit. It is interesting that the HRHD case has a reduced spanwise variation and vertical extent compared with the HR case. It also has a more effective flow recovery, as indicated by fewer low-speed streaks than the BR and HR. This flow recovery is caused by the stronger coupling between the vortex pair and the shock interaction and a reduced degree of interaction with the supersonic portion of the flow, which is a result of their reduced height and downstream placement (where the boundary layer is thicker).

Several average parameters are defined to characterize and quantify the performance of the microramps. In particular, the average incompressible displacement thickness δ^*, total-pressure recovery factor α, and incompressible shape factor H were selected. They are defined as

$$\delta^* = \int_0^{y_{\max}} 1 - \frac{U}{U^\infty}\,\mathrm{d}y \tag{14}$$

$$\theta = \int_0^{y_{\max}} \frac{U}{U^\infty}\left(1 - \frac{U}{U^\infty}\right)\mathrm{d}y \tag{15}$$

$$H = \delta^*/\theta \tag{16}$$

$$\alpha = \frac{1}{y_{\max}}\int_0^{y_{\max}} \frac{P_o}{P_o^\infty}\,\mathrm{d}y \tag{17}$$

where P_o^∞ is the freestream total pressure before the shock, and $y_{\max}$ is the distance from the wall to which the integrals are evaluated. For the RANS results, the integration height was set at $y_{\max} = y^* = 23$. This value is above the boundary layer but below the expansion wave emanating from the upper wall (recall Fig. 9). For the LES results, two different integration heights were used: $y_{\max} = y^* = 23$ to

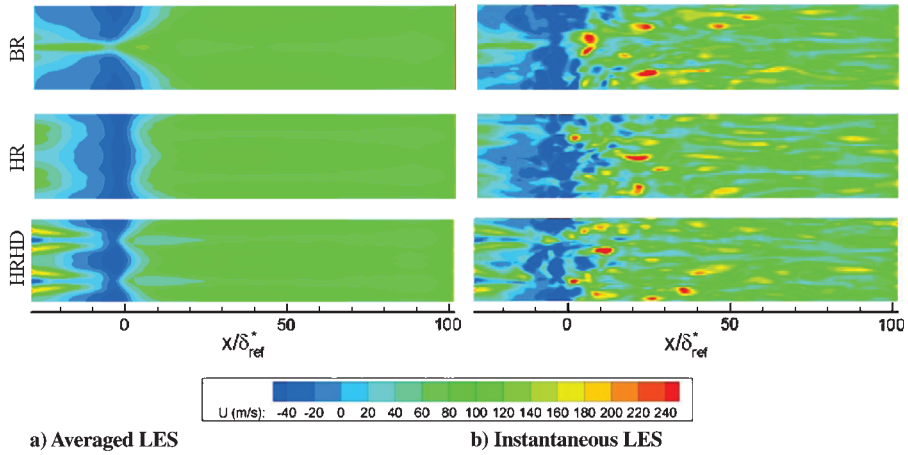

a) Averaged LES **b) Instantaneous LES**

Fig. 15 Visualization streamwise velocity from $x^* = -28.5$ to 102 at $y^+ = 1$ plane for BR, HR, and HRHD for a) averaged LES average and b) instantaneous LES.

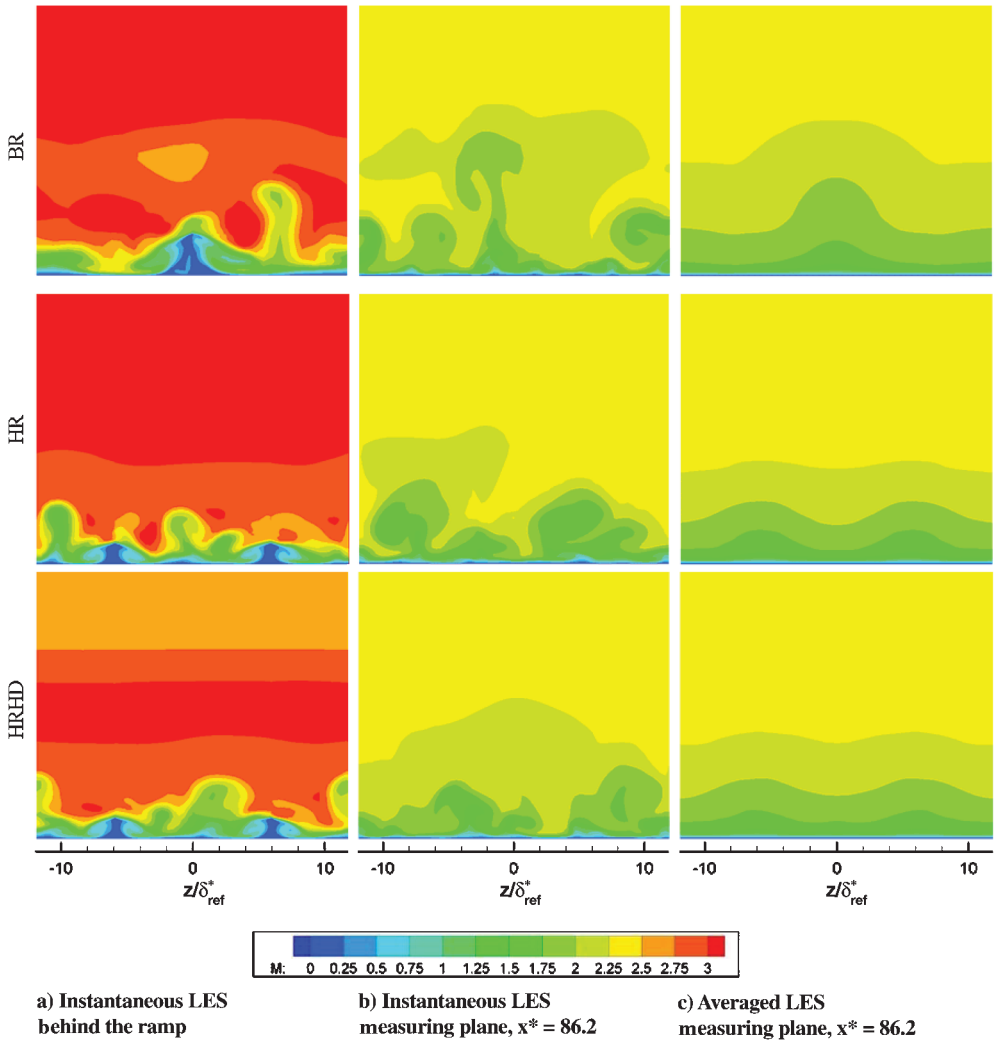

Fig. 16 Mach contours at various cross sections for BR, HR, and HRHD: a) instantaneous LES at the microramp's trailing edge ($x^* = -57$ for BR and HR and $x^* = -28.5$ for HRHD), b) instantaneous LES at measuring plane, and c) averaged LES at measuring plane.

correspond to the RANS integration and $y_{max} = y^* = 6$ to correspond to the maximum height of the pitot probe rakes in the experiments. Flow separation area A_{sep} was obtained by summing the wall areas, downstream of the microramps (in the shock interaction region) with negative wall shear stress.

Spanwise z distributions of total-pressure recovery of the BR configuration were normalized by that of the NR (α/α_{NR}) and are shown in Fig. 17a. As expected, the strongest losses are located downstream and on the microramp centerline ($z/D = 0$) and can be attributed to the wake of the ramp. To the sides of this wake are increases in the total-pressure recovery located on either side of this wake and are attributed to the high-speed flow, which is brought downward by the counter-rotating vortex pair. Further to the side, the total pressure tends toward that of the NR case. When integrated to $y^* = 23$, the LES predictions are in better agreement than RANS with the experimental data, which tended to overpredict the spanwise variations. However, consistent with differences noted in Fig. 13, the LES results integrated to $y^* = 6$ are not as accurate. The experimental boundary layer appears to be thinner than that of the LES. Similar results are found for the displacement thicknesses and shape factors and are shown in Figs. 17b and 17c. A thicker boundary layer with a larger (less healthy) H is evident on the ramp centerline for the LES results, which can be attributed to the ramp wake; the RANS predictions have much stronger spanwise variations.

Normalized total-pressure recoveries are shown in Fig. 17d as a function of the microramp configuration. In general, the HR and HRHD have a higher total-pressure recovery, which is attributed to their reduced vertical extent into the boundary layer. This effect can be seen in the larger flow disturbance combined with the shock wave generated by the BR device in the instantaneous Mach contour of Fig. 16. A decrease in the maximum displacement thickness can also be seen in the spanwise distributions of Fig. 17e for HR and HRHD. The shape factors for the BR, HR, and HRHD configurations are very similar, a fact suggesting that changes in the displacement thickness correspond to similar changes in the momentum thickness.

The average values of the performance parameters defined in Eqs. (14–17) are summarized in Table 2. Consistent with the reduced wakes noted in Fig. 17d, the smaller microramp configurations had substantially higher spanwise-averaged pressure recoveries than the NR and BR configurations. Compared with the BR configuration, there is an improvement of more than 10% in spanwise-averaged pressure; this improvement demonstrates a significant benefit of smaller microramps in controlling this particular flowfield. Improvements are also observed in the displacement thickness,

Table 2 Spanwise-averaged performance parameters[a]

Parameters	BR	HR	HRHD
α/α_{NR}	0.95	1.07	1.06
δ^*/δ^*_{NR}	1.08	1.04	1.02
H/H_{NR}	0.99	0.99	0.99
$A_{sep}/A_{sep,NR}$	1.29	0.99	0.69

[a]$\alpha_{NR} = 0.80$, $\delta^*_{NR} = 1.09\delta^*_{ref}(x_{SI})$, $H_{NR} = 1.25$, and $A_{sep,NR} = 8.01D\delta^*_{ref}$.

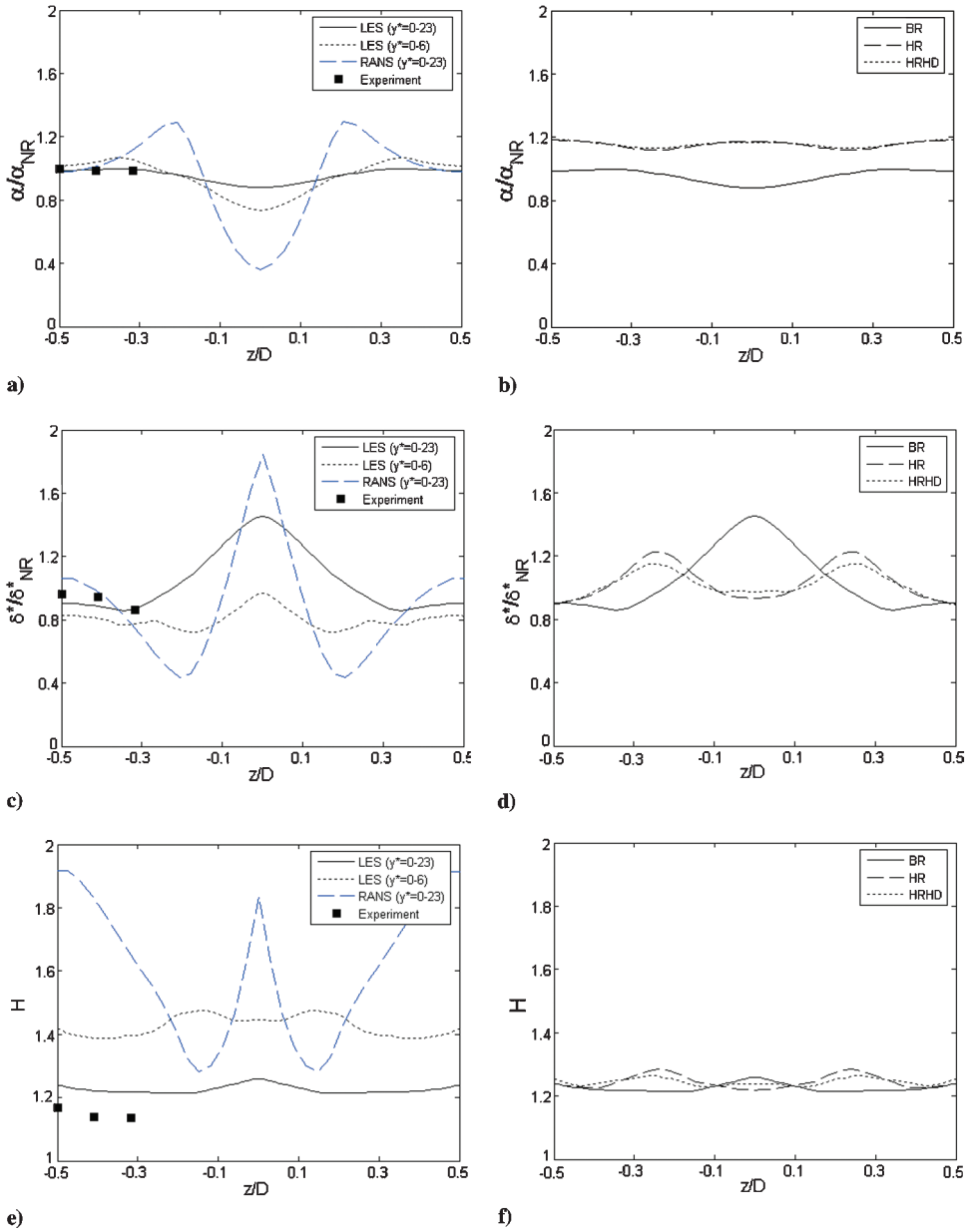

Fig. 17 Spanwise distributions of total-pressure loss (top row), displacement thickness (middle row), and incompressible shape factor (bottom row) for BR (left) and HR and HRHD (right) at measuring plane $x^* = 86.2$: a) total-pressure loss for BR and b) HR and HRHD, c) displacement thickness for BR and d) HR and HRHD, e) incompressible shape factor for BR and f) HR and HRHD.

though these values are not as small as those observed for no control (NR). Thus, the penalty paid for improved total recovery is increased boundary-layer thickness. Since the shape factors are all nearly unity, the same comments can be made with respect to the momentum thickness. The separated flow area is dramatically reduced (by more than 30%) for the HRHD configuration compared with the NR. The HR configuration showed no significant improvement in separation area. This result is attributed to reduced effectiveness of the streamwise vortices when they are generated relatively far upstream of the shock interaction region. The BR configuration yielded a larger separation region, such that the improvements in flow attachment downstream on the microramp centerline were more than offset by increases in separated flow in the outer spanwise regions. These results suggest that more investigation of the size, the location, and (possibly) the shape of the microramps are warranted to determine optimal configurations. Furthermore, the sensitivity to impinging shock strength, Mach number, and Reynolds number is also of interest and needs study to determine the effectiveness of the microramps in a range of flows.

V. Conclusions

A study of supersonic boundary-layer flow control using a microramp has been presented. The rescale–recycle algorithm for compressible flows is used to generate turbulent inflow conditions. This algorithm reduces computational cost by eliminating the need to compute boundary-layer flows from the leading edge of the flat plate. In general, the LES and RANS results captured similar fluid dynamic features of the interaction, but only the LES gave quantitative agreement with measured velocity and total-pressure profiles downstream of the interaction. In particular, the RANS results tended to overpredict the boundary-layer thicknesses, spanwise variations, and shape factors at the measuring station. However, the LES simulations required approximately a fivefold increase in computing time. With respect to the fluid physics, the shock interaction was shown to produce substantial breakup in the turbulent structures, which resulted in smaller structure aspect ratios of the structures just downstream of the shock impingement. Further downstream, the structures tended to return to their preshock characteristics. Similar results were found when a microramp was present, but the

counter-rotating vortices dominated the streamwise vorticity in the vicinity of the shock interaction and improved the overall recovery of the structures. Different sizes and locations of the microramp were also studied. Smaller microramps located at the same downstream position (HR) and located one-half of the distance to the shock impingement location (HRHD) gave qualitatively similar counter-rotating vortices, albeit with smaller scales, weaker strengths, and faster dissipation. A key benefit of the smaller ramps was their reduced incursion into the supersonic portion of the boundary layer, which reduced their overall wake effects. The smaller streamwise vortices also stayed closer to the wall. This wall proximity increased the number of near-wall high-speed streaks, especially for the HRHD configuration, for which the vortices were stronger when entering the shock interaction region. The smaller microramps yielded increased total-pressure recovery compared with the NR case. They also yielded displacement thicknesses that were smaller than the baseline ramps but larger than the NR case. A reduction of as much as 30% for the HRHD configuration over the NR was observed.

References

[1] Loth, E., "Smart Mesoflaps for Control of Shock Boundary Layer Interactions," AIAA Paper 2000-2476, 2000.

[2] Ashill, P. R., Fulker, J. L., and Hackett, K. C., "A Review of Recent Developments in Flow Control," *The Aeronautical Journal*, Vol. 109, No. 1095, May 2005, pp. 205–232.

[3] Anderson, B., Tinapple, J., and Surber, L., "Optimal Control of Shock Wave Turbulent Boundary Layer Interactions Using Micro Array Actuation," AIAA Paper 2006-3197, 2006.

[4] Garnier, E., and Sagaut, P., "Large Eddy Simulation of Shock/Boundary-Layer Interaction," *AIAA Journal*, Vol. 40, No. 10, 2002, pp. 1935–1944.
doi:10.2514/2.1552

[5] Ghosh, S., Choi, J., and Edwards, J., "RANS and Hybrid LES/RANS Simulations of the Effects of Micro Vortex Generators Using Immersed Boundary Methods," AIAA Paper 2008-3728, 2008.

[6] Clark, G. F., "Tri-Sonic Gas-Dynamic Facility User's Manual," U.S. Air Force Wright Aeronautical Lab., TM-82-176-FIMM, Dayton, OH, Apr. 1982.

[7] Lee, S., Loth, E., Wang, C., and Kim, S., "LES of Supersonic Boundary Layers μVG's," AIAA Paper 2007-3916, 2997.

[8] Fureby, C., and Grinstein, F., "Monotonically Integrated Large Eddy Simulation of Free Shear Flows," *AIAA Journal*, Vol. 37, No. 5, 1999, pp. 544–556.
doi:10.2514/2.772

[9] Urbin, G., Knight, D., and Zheltovodov, A. A., "Compressible Large-Eddy Simulation Using Unstructured Grid: Supersonic Turbulent Boundary Layer and Compression Corner," AIAA Paper 99-0427, 1999.

[10] Lund, T., Wu, X., and Squires, K., "Generation of Turbulent Inflow Data for Spatially Developing Boundary Layer Simulations," *Journal of Computational Physics*, Vol. 140, No. 2, 1998, pp. 233–258.
doi:10.1006/jcph.1998.5882

[11] Urbin, G., Knight, D., and Zheltovodov, A. A., "Large-Eddy Simulation of a Supersonic Compression Corner, Part 1," AIAA Paper 2000-0398, 2000.

[12] Loth, E., *Particles, Drops and Bubbles: Fluid Dynamics and Numerical Methods*, Cambridge Univ. Press (to be published).

[13] Kistler, A., and Chen, W., "A Fluctuating Pressure Field in a Supersonic Turbulent Boundary Layer," *Journal of Fluid Mechanics*, Vol. 16, 1963, pp. 41–64.
doi:10.1017/S0022112063000574

[14] Xu, S., and Martin, P., "Assessment of Inflow Boundary Conditions for Compressible Turbulent Boundary Layers," *Physics of Fluids*, Vol. 16, No. 7, 2004, pp. 2623–2639.
doi:10.1063/1.1758218

[15] Smits, A., and Dussauge, J. P., *Turbulent Shear Layers in Supersonic Flow*, American Inst. of Physics, New York, 1996, Chap. 2.

[16] Pirozzoli, S., and Grasso, F., "Direct Numerical Simulation of Impinging Shock Wave/Turbulent Boundary Layer Interaction at $M = 2.25$," *Physics of Fluids*, Vol. 18, No. 6, 2006, Paper 065113.
doi:10.1063/1.2216989

[17] Baldwin, B. S., and Lomax, H., "Thin Layer Approximations and Algebraic Model for Separated Turbulent Flows," AIAA Paper 78-257, 1978.

[18] Mellor, G. L., and Gibson, D. M., "Equilibrium Turbulent Boundary Layers," *Journal of Fluid Mechanics*, Vol. 24, 1966, pp. 225–253.
doi:10.1017/S0022112066000612

[19] Ganapathisubramani, B., Clemens, N. T., and Dolling, D. S., "Large-Scale Motions in a Supersonic Turbulent Boundary Layer," *Journal of Fluid Mechanics*, Vol. 556, 2006, pp. 271–282.
doi:10.1017/S0022112006009244

[20] Menter, F. R., "Two-Equation Eddy-Viscosity Turbulence Models for Engineering Applications," *AIAA Journal*, Vol. 32, No. 8, 1994, pp. 1598–1605.
doi:10.2514/3.12149

[21] Spalart, P. R., and Allmaras, S. R., "A One-Equation Turbulence Model for Aerodynamic Flows," AIAA Paper 1992-0439, 1992.

[22] Pitt Ford, C., and Babinsky. H., "MicroRamp Control for Oblique Shock Wave/Boundary Layer Interactions," AIAA Paper 2007-4115, 2007.

[23] Barber, T. J., Mounts, J. S., and McCormick, D. C., "Boundary Layer Energization by Means of Optimized Vortex Generators," AIAA Paper 1993-0445, 1993.

M. Glauser
Associate Editor